PRESEISMIC FAULT CREEP AND ELASTIC WAVE AMPLITUDE PRECURSORS SCALE WITH LAB EARTHQUAKE MAGNITUDE FOR THE CONTINUUM OF TECTONIC FAILURE MODES

Srisharan Shreedharan[1*], David Chas Bolton[1], Jacques Rivière[2], Chris Marone[1]

[1]Dept. of Geosciences, Pennsylvania State University, University Park, PA 16802 USA

[2]Dept. of Engineering Science and Mechanics, Pennsylvania State University, University Park, PA 16802 USA

***Corresponding author: srisharan@psu.edu**

Key points:

- P-wave amplitudes reduce at the onset of preseismic creep for laboratory earthquakes
- The size and onset of amplitude precursors scales with earthquake size and fault slip rate
- The microphysical mechanisms responsible for these amplitude precursors are similar for the spectrum of fault slip modes

Abstract:

Tectonic faults fail in a continuum of modes from slow earthquakes to elastodynamic rupture. Precursory variations in elastic wavespeed and amplitude, interpreted as indicators of imminent failure, have been observed in limited experimental and natural settings for this spectrum of slip modes. Such variations are thought to arise from microcracking within and around the fault zone. However, the physical mechanisms and connections to fault creep are not well understood. Here, we vary loading stiffness to generate a range of slip modes and measure fault zone properties using elastic waves transmitted through the fault. We find that elastic wave amplitudes show clear changes before failure. The temporal onset of amplitude reduction scales with lab earthquake magnitude and the magnitude of this reduction varies with fault slip. Our data suggest that continuous seismic monitoring in proximity to natural faults could be useful for assessing fault state and seismic hazard potential.

Plain Language Summary:

Earthquakes in nature can occur slowly, over many days, or rapidly within a few seconds or minutes. In a few cases geoscientists have observed, in hindsight, 'precursory' changes in seismic velocities, groundwater levels and attenuation that occurred prior to earthquakes. The ability to robustly identify these signals and accurately attribute them to imminent earthquakes could have a profound effect on our hazard preparedness, particularly for coastal communities where tsunami occur. Here, we study lab earthquakes and send acoustic pulses through laboratory faults. We show that the amplitudes of these pulses decrease systematically before failure, providing a clear precursor to failure. The magnitude of this lab earthquake precursor is related to the amount of pre-earthquake fault slip during both slow and fast laboratory earthquakes.

Introduction:

Earthquake prediction has been a longstanding goal in seismology (*Rikitake, 1968; Scholz et al., 1973; Dieterich, 1978; Geller, 1997; Hough, 2016*). Part of the difficulty is that without advanced knowledge of an impending earthquake's location, one cannot focus efforts to search for so called precursors –temporal changes in rock (or other) properties prior to failure. However, precursory variations in seismic velocity and amplitude anomalies have been observed in some cases (*Whitcomb et al., 1973; Crampin et al., 1984; Niu et al., 2008; Malagnini et al., 2019*) and lab work suggests that they might occur for the full spectrum of earthquake failure modes, from slow slip to elastodynamic earthquakes (*Main and Meredith, 1989; Sammonds et al., 1992; Kaproth and Marone, 2013; Scuderi et al., 2016*). Precursory amplitude variations, likely related to preslip, have also been observed in limited experiments on sheared rock discontinuities (*Chen et al., 1993; Hedayat et al., 2014, 2018*). Moreover, recent experimental studies have used premonitory acoustic emission (AE) signals to predict lab earthquake failure times (*Rouet-Leduc et al., 2017; Hulbert et al., 2019*). Here, we address the physical mechanisms responsible for precursors to laboratory earthquakes and focus in particular on the evolution of fault zone elastic properties as imaged by transmitted wave amplitudes.

Active and passive seismic monitoring techniques have proved promising particularly in the realm of reservoir monitoring (*Lumley et al., 2001; Zhu et al., 2019*) and in field and laboratory studies of fault frictional state, coseismic energy release and postseismic healing (*Yoshioka and Iwasa, 2006; Brenguier et al., 2008; Nagata et al., 2008; Latour et al., 2013; Aichele et al., 2018; Shreedharan et al., 2019*). The use of acoustic amplitude (or transmissivity; see Methods) is particularly appealing here since it has been demonstrated from theory and experiments (*Kendall and Tabor, 1971; Pyrak-Nolte et al., 1990; Nagata et al., 2008, Saltiel et*

65 *al., 2017; Shreedharan et al., 2019*) that transmissivity across frictional interfaces is related to
66 the stiffness and size of asperity contact junctions participating in shear. Specifically, acoustic
67 transmissivity scales with fault normal stress and healing time and inversely with slip rate during
68 steady-state shear on experimental faults (*Ryan et al., 2018; Shreedharan et al., 2019*). These
69 scaling relationships arise naturally as a result of the relationship between acoustic transmissivity
70 and asperity stiffness. Therefore, studying p-wave amplitudes enables us to directly study the
71 micro-scale physics that control the temporal variations in precursors to laboratory earthquakes.
72 However, whether resolvable precursory signals in transmissivity can be used to monitor the
73 seismogenic state of tectonic faults remains unclear, although theoretical considerations dictate
74 that it should be feasible (*Kame et al., 2014*).

75 Here, we study elastic waves propagating through frictional interfaces during the full
76 laboratory seismic cycle of loading and failure. We observe preseismic variations in acoustic
77 transmissivity linked to preslip, and demonstrate that these precursors vary systematically with
78 fault slip rate and earthquake magnitude. Our results allow us to map transmissivity and asperity
79 size, and indicate that precursors are a likely outcome of contact area reduction arising from
80 increasing local fault slip rate during a preparatory phase prior to failure.

81

82 **Methods:**

83 *Mechanical Data Acquisition*

84 Our experiments were carried out on the biaxial shear apparatus in a double direct-shear
85 (DDS) configuration in the Penn State Rock Mechanics laboratory. The apparatus was used to
86 apply normal and shear loads in the horizontal and vertical directions using two hydraulic
87 pistons. Mechanical data included output from strain gauge load cells and direct current

88 differential transformers (DCDTs) to measure normal and shear loads and displacements,
89 respectively. The strain gauge load cells, accurate to ±5 N, were calibrated with a Morehouse
90 proving ring. The DCDTs were calibrated using a Vernier height gauge and provide
91 displacement resolution of ±0.1 μm. The DCDTs were mounted on the horizontal and vertical
92 pistons (inset to Fig 1a) for far-field normal and shear displacement measurements. In addition,
93 we attached a DCDT to the central shearing block and referenced it to the base of the DDS
94 configuration to measure true fault slip. Experiments were fully servo-controlled with constant
95 normal stress and constant shear rate (far-field plate rate) boundary conditions, derived from load
96 and displacement feedback, respectively.

97 We sheared rough surfaces of Westerly granite that were coated with thin layers of quartz
98 powder (99.5% SiO_2, U.S. Silica product Min-U-Sil 40 with median grain size of 10.5 μm) to
99 simulate frictional wear material and fault gouge. Gouge layers weighed ~0.25 g and were ~250-
100 μm thick prior to the application of normal load. The granite surfaces were roughened with #60
101 grit (RMS roughness ~ 20 μm). During shear in our experiments, the gouge layers were
102 comparable in thickness to the maximum surface roughness, resulting in direct interaction
103 between the fault surfaces and additional wear (Figure S1).

104 Our sample configuration used a nominal contact area of 5 x 5 cm^2. In the DDS
105 configuration, the normal stress is applied to hold the three-block configuration together and the
106 longer central block is sheared between the stationary side blocks. All experiments were
107 conducted at room temperature and a relative humidity of 100% to ensure reproducibility.
108 Mechanical data were acquired using a 24-bit ±10 V analog-to-digital converter at 10 kHz and
109 averaged in real-time to 1000 Hz prior to saving.

All experiments were performed at a normal stress of 10 MPa and a far-field shear rate of 11 μm/s. In contrast to previous experimental works (e.g. *Leeman et al., 2016; Scuderi et al., 2016; Hulbert et al., 2019*) where the continuum of slip modes, from slow to fast frictional stick-slips, were generated by varying the normal stress on the sample, we generated the spectrum of failure modes by varying the machine loading stiffness using acrylic springs in series with the shear loading piston. This approach eliminates the possibility that differences in normal stress and in turn frictional contact area and ultrasonic amplitudes (*Shreedharan et al., 2019*) caused the effects we observe.

Within the framework of frictional slip stability (*Gu et al., 1984*), the transition from stable sliding to unstable stick-slip is a consequence of the interactions between the loading stiffness, k, and the rate of fault weakening with slip, which is given by the critical stiffness, k_c:

$$k < k_c = \frac{\sigma_{eff}(b-a)}{D_c}$$

Here, σ_{eff} is the effective normal stress imposed on the sample, a and b are rate-state friction constants and D_c is a characteristic slip distance. We vary the ratio of k/k_c to generate the full spectrum of slow and fast stick-slips (*Leeman et al., 2016)* by varying the nominal contact area of an acrylic spring in series with the loading column (Inset to Figure 1a; Figure 1b). For each experiment, the lab fault was sheared for 35 mm and shear unload-reload cycles were performed at ~2 mm and ~4 mm to measure the effective loading stiffness (*Shreedharan et al., 2019*) and to accelerate shear localization (*Frye and Marone, 2002*).

Ultrasonic Acoustic Measurements

Active ultrasonic measurements were performed using broadband (~0.02 – 2 MHz) lead-zirconate (PZT) p-polarized ultrasonic transducers (Boston Piezo-Optics Inc. PZT-5A 0.5”

compression crystals). The PZT transducers were embedded in steel plates in series with and coupled to the the DDS block configuration using molasses. Ultrasonic half-sinusoidal pulses with a frequency of 500 kHz were transmitted through the frictional interfaces at a rate of 1000 pulses per second. Each received waveform was sampled by a Verasonics high-speed digitizer at 25 MHz for ~80 μs, corresponding to a trace length of 2048 samples (Inset to Figure 1a). In this study, we use the largest peak-to-peak amplitude within the first 5 μs for ultrasonic data analyses, as highlighted in Figure 1a (yellow waveform). This wavelet represents the transducer response to the first arrival rather than the p-wave coda used by previous studies (eg. *Scuderi et al., 2016; Tinti et al, 2016; Singh et al., 2019)* which represents accumulated effects of multiple reflections through frictional interfaces and the bulk.

The raw amplitudes are then converted to transmissivity values, following previous works (*Nagata et al., 2008; Kilgore et al., 2017*). Here, Transmissivity, |T|, is the ratio of the amplitude through the DDS configuration to the amplitude through an intact block having the same length dimension. This ensures that the reported values are free from bulk deformation effects. Because each ultrasonic pulse passes through two frictional interfaces, the transmissivity reported here is the square root of the raw transmissivity (*Nagata et al., 2008; Shreedharan et al., 2019*).

Results:

We sheared rough surfaces of Westerly granite decorated with a thin coating of quartz powder to simulate earthquake fault zones. We monitored stresses, fault displacements, and fault slip rate (Fig 1) while conducting continuous ultrasonic monitoring for a range of fault slip modes, slip velocities and stress drops (refer to Supplementary Table S1 for boundary

conditions). Our experiments were designed to maintain constant frictional contact area and normal stress, which have a non-trivial effect on transmissivity (*Shreedharan et al., 2019*). Supplementary Figure S2 shows the effect of varying spring cross-sectional area on stiffness. Generally, the loading stiffness increases linearly with cross-sectional area. We observe a transition from stable sliding to quasi-dynamic and subsequently repetitive stick-slips after approximately 8-10 mm of shear (Fig. 1a). Our experiments show consistent results including, for some conditions, period-doubling (Inset to Fig. 1a) behavior with alternating slow and fast stick-slips, likely due to interactions between the gouge layers and the rough frictional interface of the granite. This observation is consistent with period-doubling observed in numerical simulations (*Gu et al., 1984*), in friction experiments when the loading stiffness is close to the critical weakening rate (*Leeman et al., 2016; Scuderi et al. 2016*) and in nature, along the San Andreas fault (*Veedu and Barbot, 2016*).

We report measurements of stress drop, peak slip velocity, slip duration and the effective machine loading stiffness for each stick-slip event (Fig. 1). Following *Leeman et al. (2016, 2018)*, we classify slow laboratory earthquakes as the instabilities without audible co-seismic energy radiation. In our experiments, slow earthquakes have stress drops of 0.3 MPa or less, maximum peak slip velocities of 300 μm/s and co-seismic durations > 0.5 s. Consistent with previous observations (*Ide et al., 2007; Peng and Gomberg, 2010; Leeman et al., 2016; Scuderi et al., 2016*), slow-slip events have consistently smaller stress drops than dynamic stick-slip instabilities. Additionally, stress drops are negatively correlated with loading stiffness, with the more compliant system producing larger, more audible instabilities (Fig. 1b). Earthquake stress drops also increase with increasing peak co-seismic slip velocities (Fig. 1c) and decrease with higher co-seismic slip durations (Fig. 1d).

A representative set of stick-slips and their associated mechanical and ultrasonic attributes are shown in Fig. 2, with Fig. 2a and Fig. 2b expressing the instabilities as functions of the imposed far-field shear displacement rate and fault slip rate respectively. We measure the coefficient of friction (hereafter referred to as friction) as the ratio of fault zone shear and normal stresses. Within the period-doubling space, slow instabilities have peak slip velocities of ~100 μm/s and fast elastodynamic events have peak slip rates of ~1 mm/s, representing an order of magnitude increase in peak slip rate (Fig. 2a). Observations of fault normal displacement indicate that the faults undergo dilation during the interseismic period (linear-elastic loading phase), begin to compact prior to failure and undergo rapid compaction during the primary stress drop as the fault slip rate reduces to near zero and the fault locks up (Fig. 2b). This indicates that compaction and reduced post-seismic slip rate could work in concert to enhance fault healing, by increasing the number and size of frictional contact junctions (*Yasuhara et al., 2005*). Ultrasonic amplitude, expressed as transmissivity, first increases during elastic loading and then decrease prior to failure for both slow and fast slip events (Fig 2a). Interestingly, the onset of preseismic transmissivity reduction also marks the onset of inelastic fault creep and an increase in fault slip rate. That is, the p-wave amplitudes decrease once the fault begins to unlock and inelastic loading occurs (Fig 2a). Subsequently, the amplitudes reduce to a minimum during the co-seismic slip phase when the fault reaches its peak slip rate (Fig. 2b).

Discussion:

Taken together, the variations in elastic wave amplitudes and fault slip during our laboratory earthquakes indicate that the precursory variations in amplitudes quantitatively track fault slip rate (Fig. 3). This observation is consistent with the long-held assertion that preslip and

nucleation zone damage could dictate the characteristics of earthquake precursors in nature (*Dieterich, 1978; Chen et al., 1993; Hedayat et al., 2014; Scholz, 2019; Acosta et al., 2019*). Broadly, variations in amplitudes observed in our experiments can be classified into two preseismic stages (Fig. 3a, e). First, the increase in wave amplitude during the linear-elastic loading phase of the interseismic period, which follows fault slip deceleration and subsequent lock-up after failure (Fig. 3a, e). During the linear-elastic loading phase, the amplitude increases logarithmically with time (Fig. 3b, f), consistent with observations of fault healing in friction experiments (*Dieterich, 1972; Ryan et al., 2018; Shreedharan et al., 2019*) and in nature (*Marone, 1998a,b; Brenguier et al., 2008*). We interpret this increase in transmissivity as an increase in the specific stiffness (see supplementary Figure S3) and strength of microscopic contact junctions that make up the granular interface, either via an increase in the number or size (or both) of asperities during the 'healing' phase (*Li et al., 2011; Shreedharan et al., 2019*).

The second stage is marked by the onset of inelastic fault creep prior to failure for fast (Fig. 3a) and slow slip events (Fig. 3e) and begins when amplitude has reached a peak value. This systematic transition from first to second stage makes transmittivity a reliable precursor to failure. Transmittivity reduces continuously during the second stage until the fault reaches its minimum shear stress during co-seismic failure, with the reduction being linear in log-time (Fig. 3c, g).

During co-seismic fault slip, the transmitted wave amplitudes attain a minimum coincident with peak fault slip rate. The maxima and minima attained by fault slip and amplitudes respectively also correspond to the peak frictional unloading rate. It is interesting to note that we observe no break in slope in the amplitude-time variation during the transition from pre- to co-seismic slip (Fig. 3c and Fig. 3e). This indicates that the contact-scale mechanics

224 controlling slip behavior may be similar for both pre- and co-seismic slip. The two-stage nature
225 of the wave amplitude precursor is consistent with previous works that documented an elastic
226 wave velocity precursor that was controlled by fault zone preslip (*Kaproth and Marone*, 2013;
227 *Scuderi et al., 2016*). When expressed as a function of logarithmic slip rate, the elastic amplitude
228 varies systematically (Fig. 3d, h). Both the increase and decrease in amplitude during the
229 interseismic period follow the same slope. Preseismic amplitude variations documented in our
230 experiments could be indicative of cascading, predictable failure (*Hulbert et al., 2019*). Thus, our
231 results suggest that continuous seismic monitoring may be used in natural settings to gather
232 insight into imminent fault failure. However, we note that extrapolating our results to field scales
233 may not be straightforward. In particular, preslip on natural faults is often small and may not
234 always be resolvable (eg. *Amoruso and Crescentini, 2009*). Additionally, at low strain rates
235 approaching those experienced by natural faults, acoustic emission foreshock precursors have
236 been observed to become temporally shorter, occurring closer to failure (*Ojala et al., 2004*).
237 Figure 4 shows the relationship between preseismic slip, co-seismic stress drops and
238 precursory amplitude reduction prior to failure. Preseismic slip is calculated here as the total slip
239 undergone, as measured by the across fault displacement transducer (Fig. 1a), between the
240 interseismic minimum shear stress and peak shear stress just before failure. Our results indicate a
241 robust relationship between elastic amplitudes and precursory slip (Fig. 4). These observations
242 are consistent with previous AE studies that have suggested that microscopic slip is related to the
243 increase in AE activity prior to stick-slips and with recent observations of precursory damage
244 prior to failure (*Niu et al., 2008; Johnson et al., 2013*).
245 Preslip has been shown to vary with both effective normal stress as well as loading rate
246 (*Scuderi et al., 2015; Leeman et al., 2018; Acosta et al., 2019*). However, the effect of fault zone

stiffness alone on preseismic slip is not well documented. Our observations of stiffness show that preslip varies inversely with stress drop magnitude (Fig. 4a) for the range of stiffnesses explored in this study. In other words, faults experiencing higher preslip release some of the accumulated strain energy via pre-seismic sliding resulting in a lower co-seismic stress drop magnitude (*Cattania and Segall, 2019*). This is consistent with the theory of time-dependent healing (*Dieterich, 1978; Marone, 1998b*) within the framework of rate-and-state friction, where higher healing is associated with an increase in subsequent seismic magnitude via an increase in real area of contact at asperity junctions. Specifically, as we increase fault zone stiffness, we observe a transitioning to stable sliding, representing infinite preslip.

Simultaneously, we calculate the reduction in preseismic amplitudes as the percent reduction from peak amplitude during elastic loading (A_{max}) to the amplitude at peak friction prior to failure (A_{cos}), referenced against the peak amplitude (Fig 3; Fig. 4b). We observe that the precursory amplitude variations are systematically higher when the fault experiences little to no preseismic slip (e.g. largest slip events). Conversely, the smallest precursory amplitude signatures are associated with the highest preseismic slip and smaller magnitude slip events. This indicates that the fault locks up more (i.e., experiences a lower interseismic minimum in slip rate) preceding ruptures with large stress drop. This allows for a higher magnitude of healing and longer healing times preceding larger co-seismic stress drops. Thus, while the onset of the precursory amplitude reduction is related to the temporal onset of preslip, the size of the amplitude precursor is intimately related to the maximum slip rate excursion experienced by the fault. This is apparent in Fig. 3a and Fig. 3d when the interseismic amplitude increases rapidly for ~2 s for the fast rupture, whereas it increases more gradually for ~0.5 s when the strain accumulation culminates in a slow earthquake (Fig. 3e). Finally, our observations of the

precursory amplitude variation indicate that the onset of the amplitude precursor occurs earlier in the seismic cycle when the fault undergoes less macroscopic preslip and the onset is delayed as the fault undergoes more preslip (Fig. 4c). The fault achieves lower slip rates earlier in the interseismic period preceding larger instabilities, and elastic wave amplitudes are related to the logarithm of the fault slip rate. Hence, the onset of small microslip precursors produces large, resolvable precursory amplitude signals earlier in the interseismic period preceding large laboratory earthquakes.

We cast the temporal onset of transmissivities in the context of natural earthquakes by converting coseismic slip into seismic moment (*Acosta et al. 2019*). We assume a shear modulus of 3 GPa for quartz gouge (*Kenigsberg et al., 2019*) and that the entire fault area (25 cm^2) ruptures which is reasonable when the fault patch is smaller than a critical nucleation length (*McLaskey and Lockner, 2014*). Our results (Figure 4d) fall remarkably close to the scaling between onset of precursors and eventual earthquake size reported by Scholz et al. (1973). This demonstrates that similar microphysical processes could operate in concert to produce precursors over multiple scales.

Conclusions and Future Directions

We report on the evolution of fault zone elastic properties throughout the laboratory seismic cycle. The transmitted wave amplitude robustly tracks precursory fault slip prior to both slow and fast laboratory earthquakes. Our observations indicate that elastic wave amplitudes are robust, scalable precursors to failure that are consistent with and higher resolution than elastic wave velocity precursors. Our data suggest that time-lapse active seismic monitoring of faults in nature could provide critical information pertinent to preslip, foreshocks and imminent failure.

293 The utility of active seismic monitoring of wave amplitude has been consistently demonstrated in
294 theoretical studies (*Kame et al., 2014*) and in limited field-based surveys such as those related to
295 CO_2 injection and storage (*Arts et al., 2004; Zhu et al., 2019*). Future research should focus on
296 applying active seismic techniques to monitor fault zones for hazard quantification and
297 mitigation (e.g., *Niu et al., 2008*). Finally, our results demonstrate the similarity between the
298 microphysical mechanisms operating before slow and fast earthquakes, which has important
299 implications to further our understanding of the mechanics of slow slip and the feedbacks
300 between the observed spectrum of tectonic slip modes.
301
302 **Acknowledgements:**
303 We thank Ake Fagereng, Ian Main and an anonymous reviewer for comments. Technical
304 assistance from laboratory manager Steve Swavely is gratefully acknowledged. This study was
305 supported by NSF-EAR1520760 , DOE Office of Basic Energy Science contract DE-
306 SC0017585, and a Schlanger Fellowship to S.S. Data are available from the PSU Scholarsphere
307 repository (https://doi.org/10.26207/12jy-rw97) or by contacting the corresponding author.
308
309

Figures:

Figure 1. The spectrum of fault slip modes generated by modifying the acrylic spring cross-sectional area (see inset). (a) Friction-displacement for a representative experiment shows the transition from stable sliding to stick-slip behavior after approximately 7 mm shear. Two unload-reload cycles are performed at ~2 mm and ~4 mm shear displacement. Left (bottom) inset shows a schematic of the double-direct shear setup with ultrasonic monitoring and slip sensor. Middle inset shows a typical ultrasonic pulse passing through the frictional interfaces with the analyzed peak-to-peak amplitudes highlighted in yellow. Right inset shows a sequence of period-doubling stick-slips and associated fault slip. (b) Static stress-drops expressed as a function of elastic loading stiffness shows an inverse trend. Colors denote different spring sizes shown in (a). Black dots represent mean values and error bars represent 1 standard deviation. (c) Peak slip velocity increases with higher stress-drops and (d) higher stress-drops are associated with lower co-seismic slip durations. In b-d, the grey region denotes silent slow laboratory earthquakes and stick-slip datasets correspond to events in the range of 18 – 21 mm.

Figure 2. Variation of fault zone dilation, slip rate and elastic amplitudes, |T|, during stick-slips. Grey boxes denote the co-seismic slip phase of a slow and fast slip event. (a) Friction drops, fault zone dilation, fault slip rate and elastic amplitudes are shown as functions of far-field imposed loading rate. Slow stick-slips are characterized by smaller stress drops than fast stick-slips for a given set of boundary conditions. During the co-seismic slip stage, the fault zone compacts, slip rate accelerates and elastic amplitudes attain a minimum value. Note that slow-slip events are also characterized by smaller peak slip velocities than faster ruptures. The preseismic reduction in amplitudes occurs during the interseismic strain accumulation phase of the stick-slip event. (b) The fault zone attributes in (a) expressed as functions of measured fault slip. Elastic amplitudes and fault zone dilation reach their respective minimum values during the maximum strain release rate portion of the co-seismic stress drop. Simultaneously, the fault slip rate reaches its maximum value.

Figure 3. The relationship between precursory amplitude variation and fault slip rate for slow (panels a-d) and fast laboratory earthquakes (panels e-h). (a) and (e) show friction (black), slip rate (green) and p-wave amplitude (purple) evolution for a representative fast and slow laboratory earthquake respectively. Note the short slip duration and large friction drop for the fast slip versus the longer transient slip duration for the slow slip. Dashed lines show the loading stiffness of the stick-slip instability. Elastic amplitudes begin to reduce at the onset of inelastic loading and continue to decrease throughout the co-seismic slip phase. (b) and (f) show the increasing limb of preseismic amplitudes expressed versus time since previous event on a logarithmic scale. The log-linear relationship of the increasing limb between amplitude and time demonstrates fault healing via contact area increase. while (c) and (g) show the reduction in amplitudes from interseismic peak to co-seismic minimum, expressed as a function of time until fault failure. (d) and (h) elastic amplitudes as a function of slip rate and colored with reference to time to failure of the next slip event. Elastic amplitudes vary log-linearly with fault slip rate. Amplitudes reduce at the onset of preseismic fault slip (see a) and continue to reduce at the same rate until they attain a minimum value during the co-seismic slip stage.

358

359 **Figure 4.** Relationship between preslip, precursors and earthquake size. (a) Static stress-drop and
360 preseismic slip are inversely related to each other for a given normal stress and imposed loading
361 rate (b) Preseismic amplitude reduction scales inversely with preseismic slip, and thus, is directly
362 correlated to the magnitude of the slip event. (c) Preseismic amplitudes reduce earlier in the
363 interseismic period for slip events with smaller amounts of preslip and larger stress drops. (d)
364 Onset of precursors increases as a function of magnitude of subsequent earthquakes showing
365 consistency across several scales.

366

367

References:

Acosta, M., Passelegue, F. X., Schubnel, A., Madariaga, R., & Violay, M. (2019). Can precursory moment release scale with earthquake magnitude? A view from the laboratory. *Geophysical Research Letters*.

Aichele, J., Catheline, S., Roux, P., Latour, S., & Voisin, C. (2018, July). Ultrafast ultrasound captures dynamic rupture behavior. In *Proceedings of Meetings on Acoustics 21ISNA* (Vol. 34, No. 1, p. 045044). ASA.

Amoruso, A., & Crescentini, L. (2009). Slow diffusive fault slip propagation following the 6 April 2009 L'Aquila earthquake, Italy. *Geophysical Research Letters*, *36*(24).

Arts, R., Eiken, O., Chadwick, A., Zweigel, P., Van der Meer, L., & Zinszner, B. (2004). Monitoring of CO2 injected at Sleipner using time-lapse seismic data. *Energy*, *29*(9-10), 1383-1392.

Brenguier, F., Campillo, M., Hadziioannou, C., Shapiro, N. M., Nadeau, R. M., & Larose, E. (2008). Postseismic relaxation along the San Andreas fault at Parkfield from continuous seismological observations. *science*, *321*(5895), 1478-1481.

Cattania, C., & Segall, P. (2019). Crack Models of Repeating Earthquakes Predict Observed Moment-Recurrence Scaling. *Journal of Geophysical Research: Solid Earth*, *124*(1), 476-503.

Chen, W. Y., Lovell, C. W., Haley, G. M., & Pyrak-Nolte, L. J. (1993, December). Variation of shear-wave amplitude during frictional sliding. In *International journal of rock mechanics and mining sciences & geomechanics abstracts* (Vol. 30, No. 7, pp. 779-784). Pergamon.

Crampin, S., Evans, R., & Atkinson, B. K. (1984). Earthquake prediction: a new physical basis. *Geophysical Journal International*, *76*(1), 147-156.

390 Dieterich, J. H. (1972). Time-dependent friction in rocks. *Journal of Geophysical*
391 *Research*, *77*(20), 3690-3697.
392 Dieterich, J. H. (1978). Preseismic fault slip and earthquake prediction. *Journal of Geophysical*
393 *Research: Solid Earth*, *83*(B8), 3940-3948.
394 Frye, K. M., & Marone, C. (2002). The effect of particle dimensionality on granular friction in
395 laboratory shear zones. *Geophysical Research Letters*, *29*(19), 22-1.
396 Geller, R. J. (1997). Earthquake prediction: a critical review. *Geophysical Journal*
397 *International*, *131*(3), 425-450.
398 Gu, J. C., Rice, J. R., Ruina, A. L., & Simon, T. T. (1984). Slip motion and stability of a single
399 degree of freedom elastic system with rate and state dependent friction. *Journal of the*
400 *Mechanics and Physics of Solids*, *32*(3), 167-196.
401 Hedayat, A., Pyrak-Nolte, L. J., & Bobet, A. (2014). Precursors to the shear failure of rock
402 discontinuities. *Geophysical Research Letters*, *41*(15), 5467-5475.
403 Hedayat, A., Haeri, H., Hinton, J., Masoumi, H., & Spagnoli, G. (2018). Geophysical Signatures
404 of Shear-Induced Damage and Frictional Processes on Rock Joints. Journal of Geophysical
405 Research: Solid Earth, 123(2), 1143-1160.
406 Hough, S. E. (2016). *Predicting the unpredictable: the tumultuous science of earthquake*
407 *prediction*. Princeton University Press.
408 Hulbert, C., Rouet-Leduc, B., Johnson, P. A., Ren, C. X., Rivière, J., Bolton, D. C., & Marone,
409 C. (2019). Similarity of fast and slow earthquakes illuminated by machine learning. *Nature*
410 *Geoscience*, *12*(1), 69.
411 Ide, S., Beroza, G. C., Shelly, D. R., & Uchide, T. (2007). A scaling law for slow
412 earthquakes. *Nature*, *447*(7140), 76.

413 Johnson, P. A., Ferdowsi, B., Kaproth, B. M., Scuderi, M., Griffa, M., Carmeliet, J., Guyer, R.
414 A., Le Bas, P-Y., Trugman, D. T., & Marone, C. (2013). Acoustic emission and microslip
415 precursors to stick-slip failure in sheared granular material. *Geophysical Research*
416 *Letters*, *40*(21), 5627-5631.
417 Kame, N., Nagata, K., Nakatani, M., & Kusakabe, T. (2014). Feasibility of acoustic monitoring
418 of strength drop precursory to earthquake occurrence. *Earth, Planets and Space*, *66*(1), 41.
419 Kaproth, B. M., & Marone, C. (2013). Slow earthquakes, preseismic velocity changes, and the
420 origin of slow frictional stick-slip. *Science*, *341*(6151), 1229-1232.
421 Kendall, K., & Tabor, D. (1971). An utrasonic study of the area of contact between stationary
422 and sliding surfaces. *Proceedings of the Royal Society of London. A. Mathematical and*
423 *Physical Sciences*, *323*(1554), 321-340.
424 Kenigsberg, A. R., Rivière, J., Marone, C., & Saffer, D. M. (2019). The effects of shear strain,
425 fabric, and porosity evolution on elastic and mechanical properties of clay-rich fault
426 gouge. *Journal of Geophysical Research: Solid Earth*, 124.
427 https://doi.org/10.1029/2019JB017944
428 Kilgore, B., Beeler, N. M., Lozos, J., & Oglesby, D. (2017). Rock friction under variable normal
429 stress. Journal of Geophysical Research: Solid Earth, 122(9), 7042-7075.
430 Latour, S., Voisin, C., Renard, F., Larose, E., Catheline, S., & Campillo, M. (2013). Effect of
431 fault heterogeneity on rupture dynamics: An experimental approach using ultrafast ultrasonic
432 imaging. *Journal of Geophysical Research: Solid Earth*, *118*(11), 5888-5902.
433 Leeman, J. R., Saffer, D. M., Scuderi, M. M., & Marone, C. (2016). Laboratory observations of
434 slow earthquakes and the spectrum of tectonic fault slip modes. *Nature communications*, *7*,
435 11104.

436 Leeman, J. R., Marone, C., & Saffer, D. M. (2018). Frictional mechanics of slow
437 earthquakes. *Journal of Geophysical Research: Solid Earth*, *123*(9), 7931-7949.
438 Li, Q., Tullis, T. E., Goldsby, D., & Carpick, R. W. (2011). Frictional ageing from interfacial
439 bonding and the origins of rate and state friction. *Nature*, *480*(7376), 233.
440 Lumley, D. E. (2001). Time-lapse seismic reservoir monitoring. *Geophysics*, *66*(1), 50-53.
441 Main, I. G., & Meredith, P. G. (1989). Classification of earthquake precursors from a fracture
442 mechanics model. *Tectonophysics*, *167*(2-4), 273-283.
443 Malagnini, L., Dreger, D. S., Bürgmann, R., Munafò, I., & Sebastiani, G. (2019). Modulation of
444 seismic attenuation at Parkfield, before and after the 2004 M6 earthquake. *Journal of*
445 *Geophysical Research: Solid Earth*.
446 Marone, C. (1998a). Laboratory-derived friction laws and their application to seismic
447 faulting. *Annual Review of Earth and Planetary Sciences*, *26*(1), 643-696.
448 Marone, C. (1998b). The effect of loading rate on static friction and the rate of fault healing
449 during the earthquake cycle. *Nature*, *391*(6662), 69.
450 McLaskey, G., & Lockner, D. A. (2014). Preslip and cascade processes initiating laboratory stick
451 slip. Journal of Geophysical Research: Solid Earth, 119, 6323–6336.
452 https://doi.org/10.1002/2014JB011220
453 Nagata, K., Nakatani, M., & Yoshida, S. (2008). Monitoring frictional strength with acoustic
454 wave transmission. Geophysical Research Letters, 35(6).
455 Niu, F., Silver, P. G., Daley, T. M., Cheng, X., & Majer, E. L. (2008). Preseismic velocity
456 changes observed from active source monitoring at the Parkfield SAFOD drill
457 site. *Nature*, *454*(7201), 204.

458 Ojala, I. O., Main, I. G., & Ngwenya, B. T. (2004). Strain rate and temperature dependence of
459 Omori law scaling constants of AE data: Implications for earthquake foreshock-aftershock
460 sequences. *Geophysical Research Letters*, *31*(24).
461 Peng, Z., & Gomberg, J. (2010). An integrated perspective of the continuum between
462 earthquakes and slow-slip phenomena. *Nature geoscience*, *3*(9), 599.
463 Pyrak-Nolte, L. J., Myer, L. R., & Cook, N. G. (1990). Transmission of seismic waves across
464 single natural fractures. *Journal of Geophysical Research: Solid Earth*, *95*(B6), 8617-8638.
465 Rikitake, T. (1968). Earthquake prediction. *Earth-Science Reviews*, *4*, 245-282.
466 Rouet-Leduc, B., Hulbert, C., Lubbers, N., Barros, K., Humphreys, C. J., & Johnson, P. A.
467 (2017). Machine learning predicts laboratory earthquakes. *Geophysical Research*
468 *Letters*, *44*(18), 9276-9282.
469 Ryan, K. L., Rivière, J., & Marone, C. (2018). The Role of Shear Stress in Fault Healing and
470 Frictional Aging. *Journal of Geophysical Research: Solid Earth*, *123*(12), 10-479.
471 Saltiel, S., Selvadurai, P. A., Bonner, B. P., Glaser, S. D., & Ajo-Franklin, J. B. (2017).
472 Experimental development of low-frequency shear modulus and attenuation measurements in
473 mated rock fractures: Shear mechanics due to asperity contact area changes with normal
474 stress. *Geophysics*, *82*(2), M19-M36.
475 Sammonds, P. R., Meredith, P. G., & Main, I. G. (1992). Role of pore fluids in the generation of
476 seismic precursors to shear fracture. *Nature*, *359*(6392), 228.
477 Scholz, C. H., Sykes, L. R., & Aggarwal, Y. P. (1973). Earthquake prediction: a physical
478 basis. *Science*, *181*(4102), 803-810.
479 Scholz, C. H. (2019). *The mechanics of earthquakes and faulting*. Cambridge university press.

480 Scuderi, M. M., Marone, C., Tinti, E., Di Stefano, G., & Collettini, C. (2016). Precursory
481 changes in seismic velocity for the spectrum of earthquake failure modes. *Nature*
482 *geoscience*, *9*(9), 695.
483 Shreedharan, S., Rivière, J., Bhattacharya, P., & Marone, C. (2019). Frictional State Evolution
484 during Normal Stress Perturbations Probed with Ultrasonic Waves. *Journal of Geophysical*
485 *Research: Solid Earth*.
486 Singh, J., Curtis, A., Zhao, Y., Cartwright-Taylor, A., & Main, I. (2019). Coda Wave
487 Interferometry for Accurate Simultaneous Monitoring of Velocity and Acoustic Source
488 Locations in Experimental Rock Physics. *Journal of Geophysical Research: Solid Earth*.
489 Tinti, E., Scuderi, M. M., Scognamiglio, L., Di Stefano, G., Marone, C., & Collettini, C. (2016).
490 On the evolution of elastic properties during laboratory stick-slip experiments spanning the
491 transition from slow slip to dynamic rupture. *Journal of Geophysical Research: Solid*
492 *Earth*, *121*(12), 8569-8594.
493 Veedu, D. M., & Barbot, S. (2016). The Parkfield tremors reveal slow and fast ruptures on the
494 same asperity. *Nature*, *532*(7599), 361.
495 Whitcomb, J. H., Garmany, J. D., & Anderson, D. L. (1973). Earthquake prediction: Variation of
496 seismic velocities before the San Francisco earthquake. *Science*, *180*(4086), 632-635.
497 Yasuhara, H., Marone, C., & Elsworth, D. (2005). Fault zone restrengthening and frictional
498 healing: The role of pressure solution. *Journal of Geophysical Research: Solid*
499 *Earth*, *110*(B6).
500 Yoshioka, N., & Iwasa, K. (2006). A laboratory experiment to monitor the contact state of a fault
501 by transmission waves. *Tectonophysics*, *413*(3-4), 221-238.

502 Zhu, T., Ajo-Franklin, J., Daley, T. M., & Marone, C. (2019). Dynamics of geologic CO_2 storage
503 and plume motion revealed by seismic coda waves. *Proceedings of the National Academy of*
504 *Sciences*, *116*(7), 2464-2469.

Figure 1.

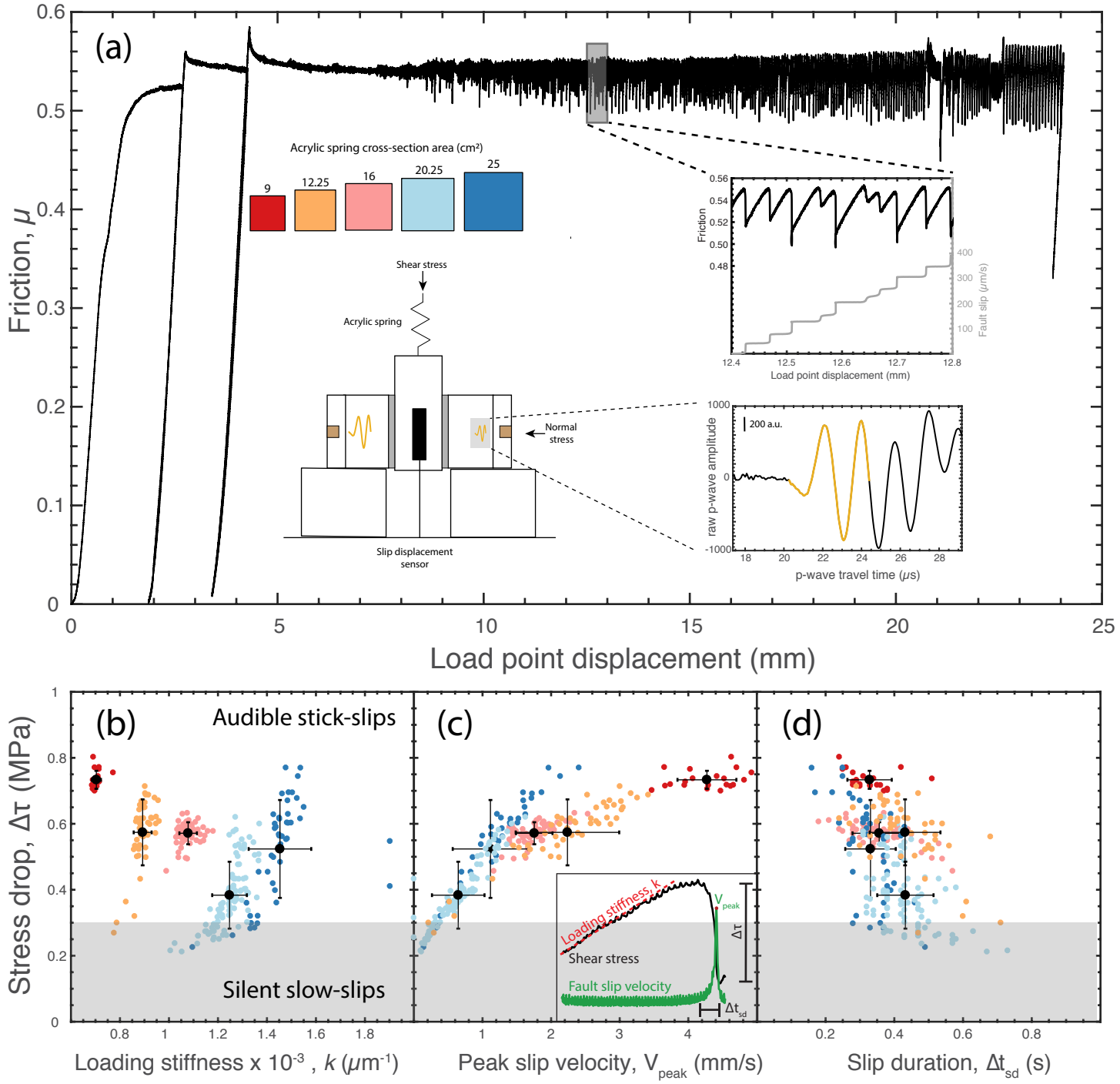
(a)
Friction, μ
Load point displacement (mm)
Acrylic spring cross-section area (cm²)
9
12.25
16
20.25
25
Shear stress
Acrylic spring
Normal stress
Slip displacement sensor
Friction
Fault slip (μm/s)
Load point displacement (mm)
raw p-wave amplitude
200 a.u.
p-wave travel time (μs)

(b)
Audible stick-slips
Silent slow-slips
Stress drop, Δτ (MPa)
Loading stiffness x 10⁻³ , k (μm⁻¹)
(c)
Loading stiffness, k
Shear stress
Fault slip velocity
V peak
Δτ
Δt sd
Peak slip velocity, V peak (mm/s)
(d)
Slip duration, Δt sd (s)

Figure 2.

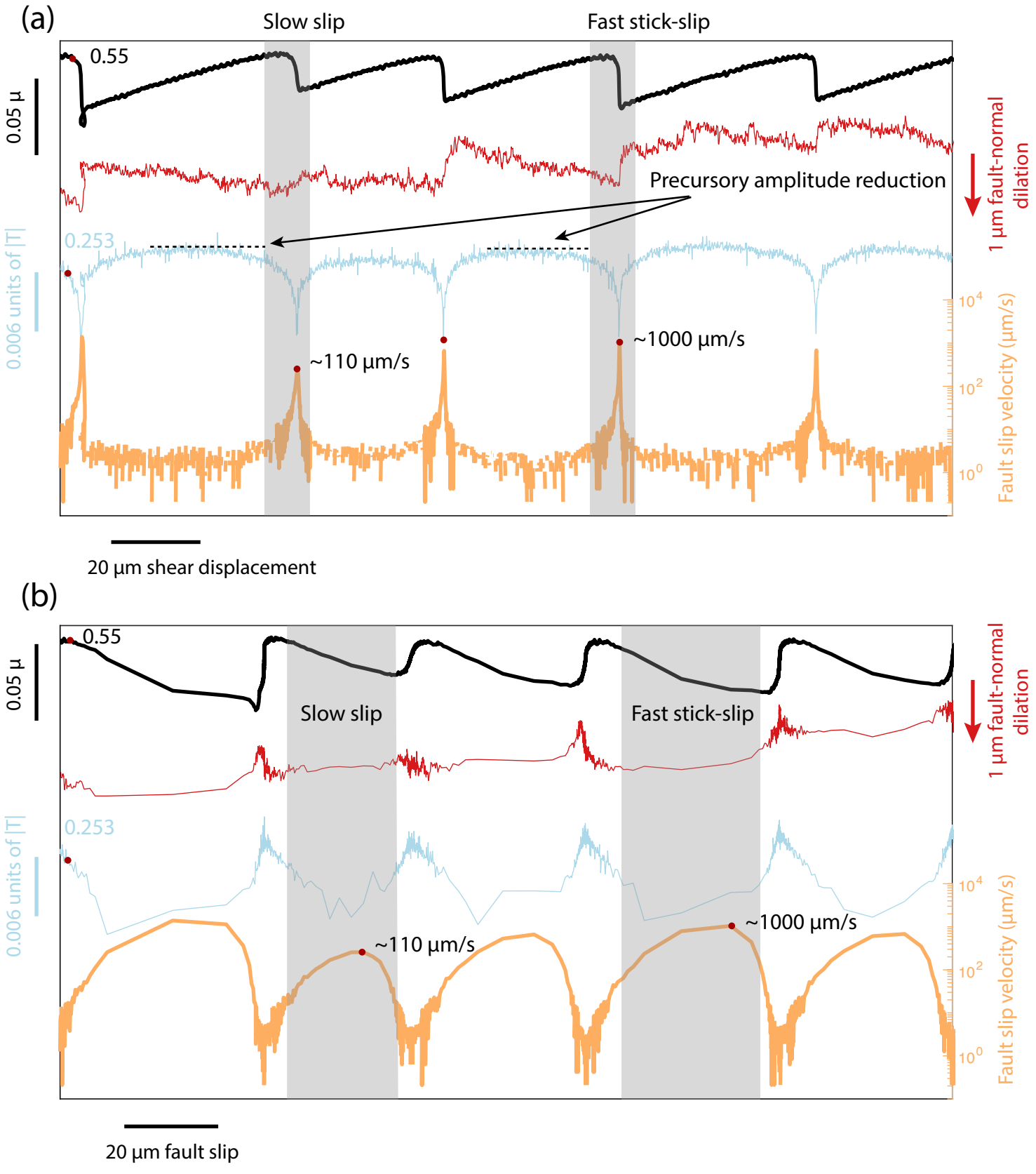
(a)
Slow slip
Fast stick-slip
0.55
0.05 μ
Precursory amplitude reduction
1 μm fault-normal dilation
0.253
0.006 units of |T|
~110 μm/s
~1000 μm/s
Fault slip velocity (μm/s)
20 μm shear displacement
(b)
0.55
0.05 μ
Slow slip
Fast stick-slip
1 μm fault-normal dilation
0.253
0.006 units of |T|
~110 μm/s
~1000 μm/s
Fault slip velocity (μm/s)
20 μm fault slip

Figure 3.

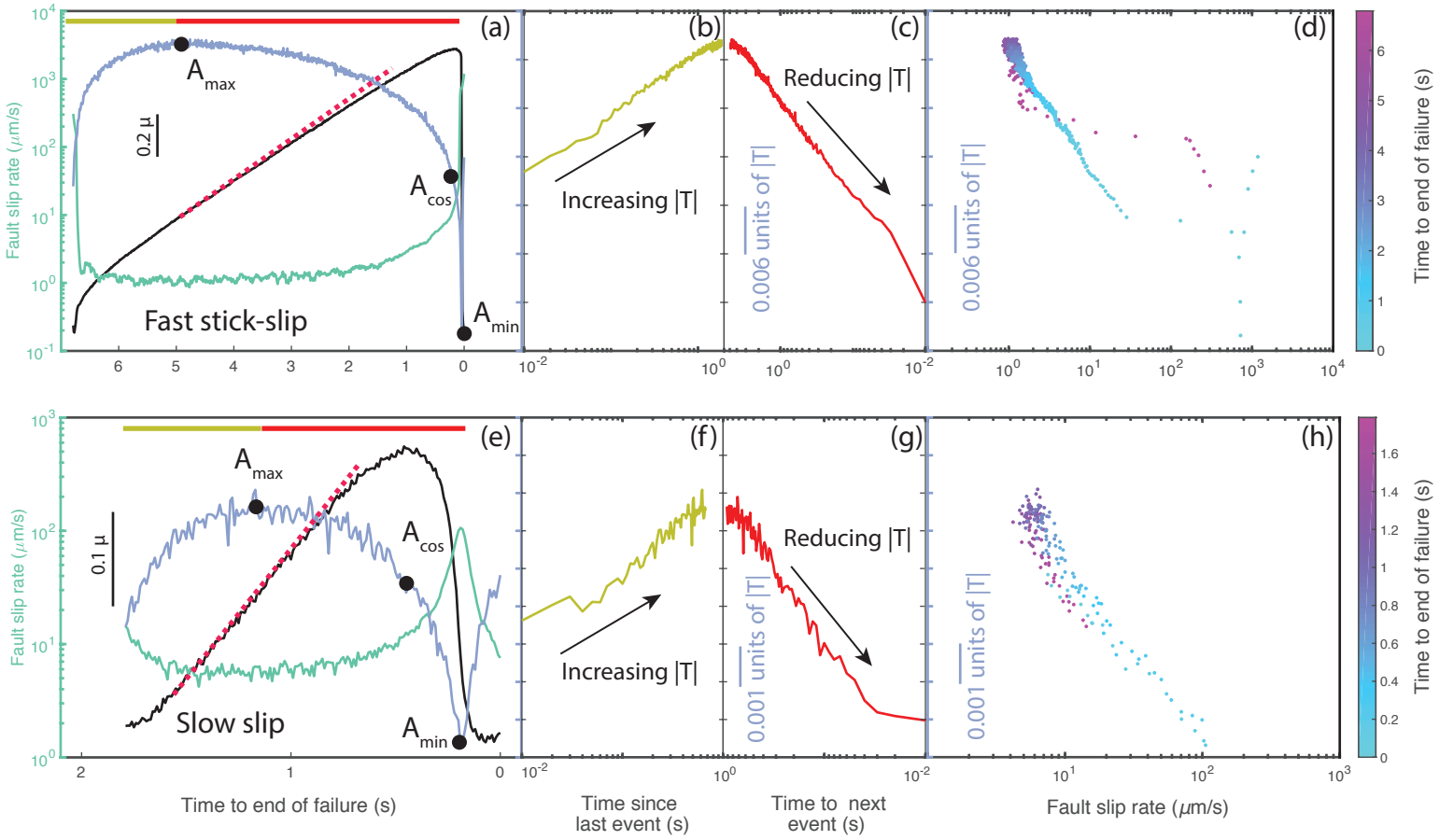
(a)
(b)
(c)
(d)
(e)
(f)
(g)
(h)
A max
A cos
A min
0.2 μ
0.1 μ
Fast stick-slip
Slow slip
Increasing |T|
Reducing |T|
0.006 units of |T|
0.001 units of |T|
Fault slip rate (μm/s)
Time to end of failure (s)
Time since last event (s)
Time to next event (s)
Fault slip rate (μm/s)
Time to end of failure (s)

Figure 4.

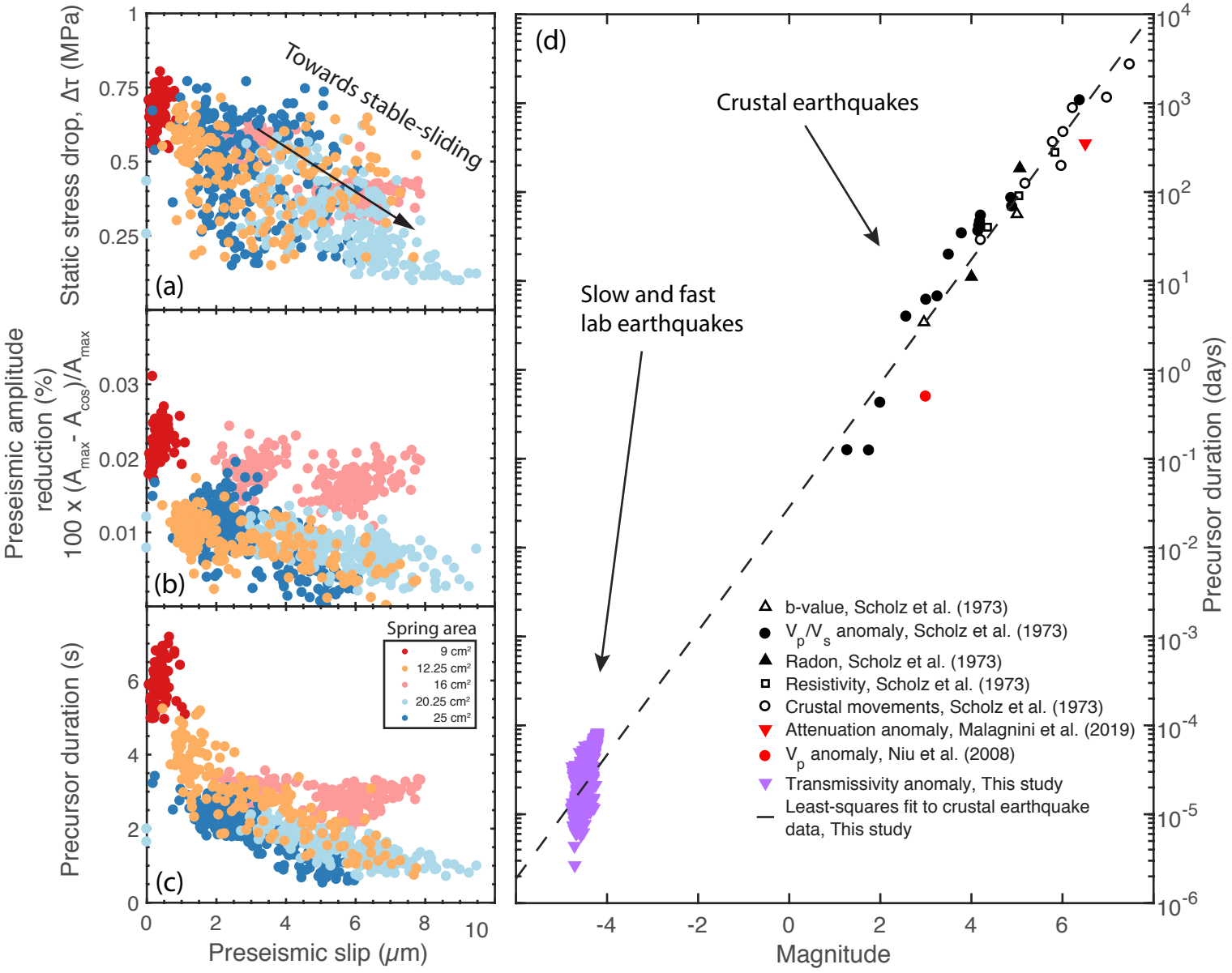
Static stress drop, Δτ (MPa)
Towards stable-sliding
(a)
Preseismic amplitude reduction (%)
100 x (A_max - A_cos)/A_max
(b)
Precursor duration (s)
Spring area
9 cm²
12.25 cm²
16 cm²
20.25 cm²
25 cm²
(c)
Preseismic slip (μm)
(d)
Crustal earthquakes
Slow and fast lab earthquakes
b-value, Scholz et al. (1973)
V_p/V_s anomaly, Scholz et al. (1973)
Radon, Scholz et al. (1973)
Resistivity, Scholz et al. (1973)
Crustal movements, Scholz et al. (1973)
Attenuation anomaly, Malagnini et al. (2019)
V_p anomaly, Niu et al. (2008)
Transmissivity anomaly, This study
Least-squares fit to crustal earthquake data, This study
Magnitude
Precursor duration (days)